Mechanisms of Neutron Irradiation Hardening in Impurity-Doped Ferritic Alloys

Y. NISHIYAMA, X.Y. LIU, and J. KAMEDA

Mechanisms of neutron irradiation hardening in phosphorus (P)-doped, sulfur (S)-doped, and copper (Cu)-doped ferritic alloys have been studied by applying a rate theory to the temperature dependence of the yield strength. Hardening behavior induced by neutron irradiation at various temperatures (473 to 711 K) is characterized in terms of the variations in athermal stress and activation energy for plasticity controlled by precipitation or solid solution, and kink-pair formation with the content and type of impurities. In P-doped alloys, neutron irradiation below 563 K brings about a remarkable increase in the athermal stress and activation energy, due to the dispersion of fine (~1.7-nm) P-rich precipitates that is more extensive than that for the Cu-rich precipitates reported in irradiated steel. During neutron irradiation above 668 K, precipitation hardening occurs to some extent in Cu-doped and S-doped alloys, compared to small or negligible hardening in the P-doped alloys. In alloys with a low to moderate content of various dissolved impurities subjected to high-temperature irradiation, the formation of kink pairs becomes considerably difficult. Differing dynamic interactions of dissolved and precipitated impurities, *i.e.*, P and Cu, with the nucleation and growth of dislocations are discussed, giving rise to irradiation hardening.

DOI: 10.1007/s11661-008-9482-9

I. INTRODUCTION

NEUTRON irradiation embrittlement leading to an increase in the ductile-brittle transition temperature (DBTT) proceeds in aging nuclear reactor pressure vessel (RPV) steels and impurity-doped ferritic alloys, due to hardening[1–4] and intergranular phosphorus (P) segregation.[3,5–8] Irradiation hardening, which facilitates the growth of a brittle crack by suppressing dislocation activities near the crack tip, is a common problem for a variety of RPV steels, and P segregation weakens grain boundaries in RPV steels such as the C-Mn steel and the $2\frac{1}{4}$Cr-1Mo steel, but does not produce much grain-boundary weakening in the A533B steel.

High-purity (HP) A533B steels, neutron irradiated to a high fluence of 1.1×10^{24} n/m^2, reveal weak hardening caused by defect clustering.[4] Meanwhile, strong interactions of neutron-irradiation-induced defects with metalloids and metallic impurities lead to nonequilibrium phase transformation, that is, the formation of nanosized precipitates[2,3] the dispersion of which causes irradiation hardening. In neutron-irradiated RPV steels, copper (Cu) becomes the nuclei of the ultrafine precipitates, combined with alloying elements of manganese (Mn), nickel (Ni), and silicon (Si).[3] Increasing the irradiation fluence results in an increased density of Cu-rich precipitates and suppresses the coarsening that usually occurs under prolonged thermal aging. Atomistic molecular dynamic simulation[9] has demonstrated that peculiar precipitation behavior under neutron irradiation is ascribed to the dragging effect of copper and vacancy fluxes. Likewise, the presence of phosphorus is found to promote irradiation hardening in ferritic alloys and RPV steels, although the mechanism is not sufficiently known.[6,10–14]

The DBTT shift in neutron-irradiated ferritic alloys is related to the temperature dependence of the hardening behavior. However, irradiation hardening behavior has generally been studied at ambient temperatures as a function of irradiation fluence rather than of irradiation temperature. As shown in Figure 1, two mechanisms controlling dislocation motion through a field of discrete obstacles (DOs), *i.e.*, solid solution or precipitation and lattice resistance (LR), dominate in high- and low-temperature ranges, respectively.[15–17] Therefore, an investigation into the effect of neutron irradiation on DO- and LR-controlled hardening is necessary in alloys with precipitated and dissolved impurities. To gain a better understanding of the hardening mechanism, in particular, it is important to examine how the neutron irradiation temperature influences the plasticity.

This study is undertaken to clarify hardening mechanisms under neutron irradiation at 473 to 711 K in varying ferritic alloys doped with P, Cu, sulfur (S), Ni, and/or Mn. By analyzing the temperature dependence of the yield stress (σ_y) using a rate theory, irradiation-hardening behavior is examined in terms of the athermal

Y. NISHIYAMA, Research Scientist, is with the Japan Atomic Energy Agency, Tokai, Ibaraki 319, Japan. X.Y. LIU, Research Associate, is with the Department of Materials Science and Engineering, University of Pennsylvania, Philadelphia. J. KAMEDA, Senior Scientist, Structural Integrity Associates, Inc., Annapolis, MD 21401, is Senior Fellow, Department of Materials Science and Engineering, University of Pennsylvania, Philadelphia, PA 19104. Contact e-mail: kamedaj@seas.upenn.edu

Manuscript submitted September 17, 2007.
Article published online March 21, 2008

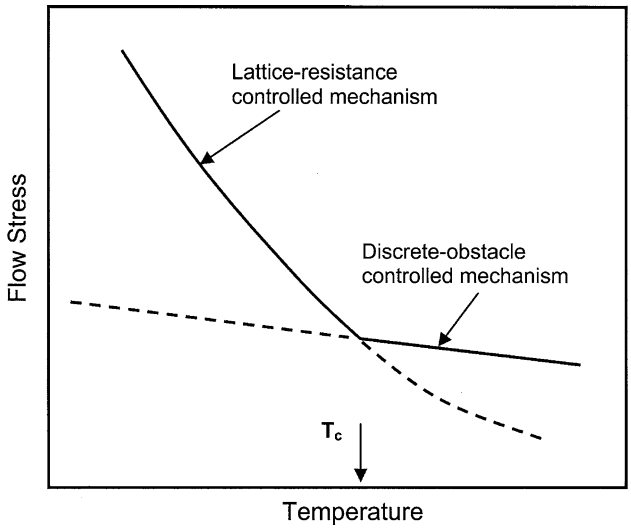

Fig. 1—Schematic drawing of temperature dependence of yield stress, indicating the mechanism transition from DO- to LR-controlled plasticity at T_c.

stress and activation energy for DO- and LR-controlled plasticity, which are related to the content and type of impurities. A comparison of the present findings, including small-angle neutron scattering (SANS) analysis of irradiation-induced P-rich precipitate, with other investigations[3,18–21] shows how phosphorus and copper affect solid solution and precipitation hardening during thermal treatment and neutron irradiation. Different dynamic interactions between irradiation-induced defects and impurities in the grain interior and near grain boundaries are discussed; these play a crucial role in hardening and intergranular segregation.[13]

II. MATERIALS AND EXPERIMENTAL PROCEDURES

A. *Impurity-Doped Ferritic Alloys and Neutron Irradiation Conditions*

Materials used in this article were three groups of impurity-doped ferritic alloys. Group I consists of Cu-doped (CUD), P-doped (PD), and Cu-P-doped (CUPD) alloys. Group II is manganese-containing alloys doped with different levels of phosphorus, and an S-doped (SD) alloy without Mn. The alloys doped with phosphorus of 0.016, 0.117, and 0.38 wt pct are designated as low P-doped (PL), moderately P-doped (PM), and highly P-doped (PH). Group III is comprised of Mn-P-doped (MA), Mn-P-Cu-doped (MCu), and Mn-P-Ni-doped (MNi) alloys. The chemical compositions of the various alloys are shown in Table I. The square root of the atomic percent of phosphorus, sulfur, and copper ($\sqrt{C_P}$, $\sqrt{C_S}$, and $\sqrt{C_{Cu}}$) is compared in the group I through III alloys (Figure 2); this is related to the inverse obstacle spacing controlling the dislocation motion[21] (Appendix I). The P content of the PD, CUPD, and group III alloys is similar. The contents of Cu and S in the CUD and SD alloys are similar to the P content of the PM and PL alloys, respectively. The amounts of interstitial impurities, *i.e.*, carbon, nitrogen and oxygen, changed in an uncontrolled manner. The content of interstitial impurities tends to increase in the group II, III, and I alloys, in that order. All the alloys were recrystallized at 1123 to 1223 K for 1 to 2 hours and annealed at 873 K for 1 to 2 hours, followed by water quenching or furnace cooling, with a relatively fast cooling rate of 1.7 K/s in the range of 873 to 473 K. The grain size varied over a range of 85 to 150 μm.

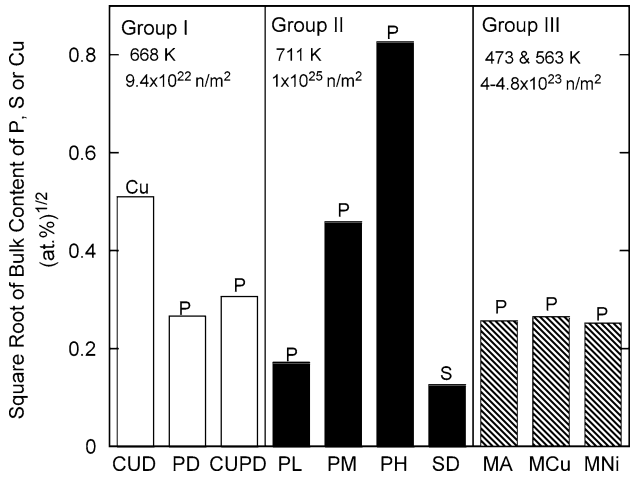

Fig. 2—Comparisons of square root of bulk content of P, S and Cu (at. pct)$^{1/2}$, representing the inverse obstacle spacing, in various alloy groups.

Table I. Chemical Compositions of Various Impurity-Doped Ferritic Alloys (Groups I through III) (Weight Percent); Bold Numbers Indicate Doping Content of P, S, Cu, and Ni

IRR Group	Alloys	Mn	Cu	Ni	P	S	C	O	N
Group I	CUD	—	**0.2957**	—	0.0039	0.0020	0.0007	0.0035	0.0025
	PD	—	0.0011	—	**0.0392**	0.0016	0.0012	0.0047	0.0016
	CUPD	—	**0.2971**	—	**0.0520**	0.0019	0.0008	0.0072	0.0020
Group II	PL	0.0275	—	—	**0.0163**	—	0.0011	0.0213	0.0004
	PM	0.0295	—	—	**0.117**	—	0.0027	0.0347	—
	PH	0.0356	0.0302	—	**0.380**	0.0037	0.0019	0.0239	0.0014
	SD	—	—	—	0.0013	**0.0091**	0.0006	0.0416	—
Group III	MA	1.18	—	—	**0.0364**	0.002	0.0011	0.0104	0.0002
	MCu	1.15	**0.29**	—	**0.039**	0.002	0.001	0.0102	0.0009
	MNi	1.16	—	**0.61**	**0.0348**	0.002	0.0008	0.0137	0.001

Table II. Conditions of Neutron Irradiation and Strain Rate ($d\varepsilon/dt$) of Impurity-Doped Alloys in Groups I through III

Alloys	$d\varepsilon/dt$ (s^{-1})	Reactor	Fluence (n/m^2)	Temperature	Duration (h)	Energy
Group I	2.7×10^{-3}	LTR	9.4×10^{22}	668 K	127	> 0.1 MeV
Group II	1.1×10^{-3}	EBR-II	1.0×10^{25}	711 K	2120	> 0.1 MeV
Group III	4.3×10^{-4}	JMTR	4 and 4.8×10^{23}	473 and 563 K	1067 and 1179	> 1 MeV

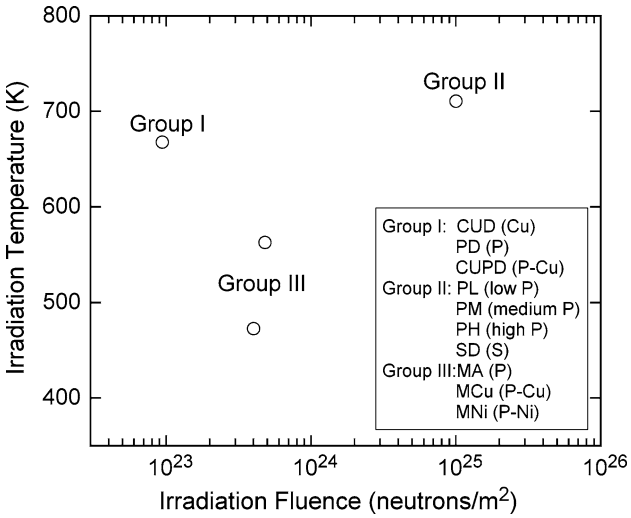

Fig. 3—Plot of neutron irradiation temperature against fluence for three alloy groups. For the various alloys, doping elements are indicated.

The three alloy groups were neutron irradiated under different conditions of temperature and fluence, using materials testing reactors, *i.e.*, the LTR at Oak Ridge National Laboratory (Oak Ridge, TN),[5,10] the EBR-II at the Idaho National Laboratory (Idaho Falls, ID),[11,12] and the JMTR at the Japan Atomic Energy Agency (Tokai, Ibaraki, Japan)[13] (Table II). As shown in a plot of the irradiation temperature against the neutron fluence (Figure 3), the group I and II alloys were irradiated by fast neutrons to low and high fluences (9.4×10^{22} and 10^{25} n/m^2) above 668 K. The group III alloys were neutron irradiated by the intermediate fluence of 4 to 4.8×10^{23} n/m^2 at 473 and 563 K. Because the impurity-doped alloys are exposed to various conditions of neutron irradiation, it is possible to know whether the irradiation temperature or fluence is the more dominant factor in controlling irradiation hardening. The group II alloys were subject to thermal aging (ETA) equivalent to the neutron irradiation condition. Intergranular impurity segregation in these unirradiated (UN) and irradiated (IRR) alloys has been studied elsewhere.[5,11–13]

B. *Small Punch Testing Method*

Small punch specimens with a 10-mm-square or 8-mm-disk diameter and a 0.5-mm thickness (t_o) of various unirradiated, irradiated, and aged alloys were clamped using a lower and upper die and four screws.[22,23] Axisymmetric punch loading was applied, to examine the deformation behavior at different temperatures. Small punch tests of the three alloy groups were conducted using different crosshead speeds ($d\delta/dt$) in a wide range of testing temperatures from 77 to 523 K, in a bath of liquid nitrogen, mixed isopentane, and liquid nitrogen or silicon oil. From the load-*vs*-deflection curves, the yield load (P_y) is defined at the transition from the elastic-to-plastic bending deformation.[23,24] The yield strength (σ_y) can be empirically determined using

$$\sigma_y \text{ (MPa)} = 360 \ (P_y/t_o^2) \text{ (kN/mm}^2\text{)} \qquad [1]$$

The strain rate ($d\varepsilon/dt$) is estimated by taking a derivative of the relation between the strain and displacement ($\varepsilon = 0.12(\delta/t_o)^{1.72}$) with respect to the time:[24]

$$d\varepsilon/dt = 0.206 \left(\delta_y^{0.72}/t_o^{1.72}\right)(d\delta/dt) \qquad [2]$$

where the average value of the yielding displacement (δ_y) is ~0.1 ± 0.03 mm. The strain rates estimated using Eq. [2] for the group I (CUD, PD, and CUPD), group II (PL, PM, PH, and SD), and group III (MA, MCu, and MNi) alloys were 2.7×10^{-3}, 1.1×10^{-3}, and 4.3×10^{-4} s^{-1}, respectively. The σ_y of high-purity iron cited in this article was obtained in tension under $d\varepsilon/dt = 8.3 \times 10^{-5}$ s^{-1}.[25]

C. *Small-Angle Neutron Scattering Analysis*

The volume fraction (f_v) and diameter (d) of precipitates in MA alloys irradiated at 473 and 563 K were analyzed using the NG7-30m SANS instrument at the National Institute of Standards and Technology (NIST) Center for Neutron Research (Gaithersburg, MD).[26] Since domain walls produce SANS in a ferromagnetic material, a 2-tesla magnetic field was applied in a horizontal direction perpendicular to the neutron beam during measurement of the neutron scattering intensity as a function of the scattering vector. The details of the SANS analysis are described in Appendix II.[27,28]

III. PLASTIC DEFORMATION BEHAVIOR

A. *Rate-Controlling Plasticity and Temperature Dependence of Yield Stress*

A rate theory is applied, to analyze the effects of precipitated and dissolved impurities on the nucleation and growth of dislocations; these govern the mechanism of irradiation hardening in impurity-doped ferritic alloys. The rate equations are described in Appendix I, in accordance with the deformation-mechanism maps presented by Frost and Ashby.[15] There are two

plasticity mechanisms controlled by the dislocation movement through discrete obstacles and lattice resistance, which are related to the weak and strong temperature dependence, respectively, of the flow stress (Figure 1). It is noted that LR-controlled plasticity is limited by the nucleation of kink pairs. In the rate theory, the athermal stress (σ_a^i) and activation energy (ΔF^i) are physical parameters characterizing the plasticity mechanism (superscript of $i = o$: DO-controlled plasticity and $i = l$: LR-controlled plasticity). The ΔF^o and ΔF^l represent the strength of a single obstacle and the formation energy of an isolated kink pair, respectively. The athermal stresses (σ_a^o and σ_a^l) in the absence of the thermal energy are reflected not only by the obstacle strength and the kink-pair formation but also by the spacing of the discrete obstacles and the density of the kink-pair nucleation sites.

The rate equation for DO- and LR-controlled plasticity describes the linear and nonlinear temperature dependence of the σ_y (Appendix I). For DO-controlled plasticity, the athermal stress and activation energy can be defined in Eqs. [3] and [4], derived from Eq. [AI-6]:

$$\sigma_y = \sigma_a^o - \psi T \qquad [3]$$

$$\Delta F^o = \left(\sigma_a^o \mathrm{R}/\psi\right) \ln\left\{\sqrt{3} \times 10^{-6} (d\varepsilon/dt)\right\} \qquad [4]$$

where ψ is the gradient of the yield stress with respect to the absolute temperature (T) and R is the gas constant. Using Eqs. [AI-7] and [AI-8], the rate equation for LR-controlled plasticity is given in a complex form:

$$\left[2RT\ln\left\{\sigma_y/(2050-0.81T)\right\} - RT\ln\left(1.54\times 10^7 d\varepsilon/dt\right)\right]^{3/4} = \left(\Delta F^l\right)^{3/4}\left\{1-\left(\sigma_y/\sigma_a^l\right)^{3/4}\right\} \qquad [5]$$

The left side of Eq. [5] includes the experimental conditions and observation (T, $d\varepsilon/dt$, and σ_y), and the right side represents the physical parameters (ΔF^l and σ_a^l) to be estimated.

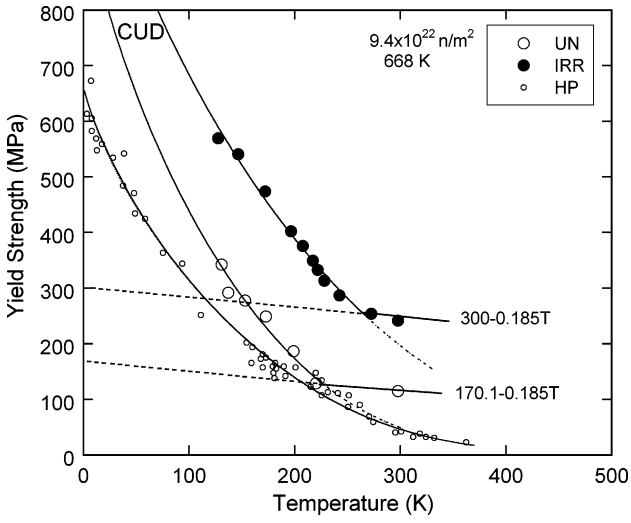

Fig. 4—Temperature dependence of yield strength (σ_y) for UN and IRR Cu-doped alloys, compared with that of HP iron. The data are fitted to rate equations representing linear and nonlinear curves.

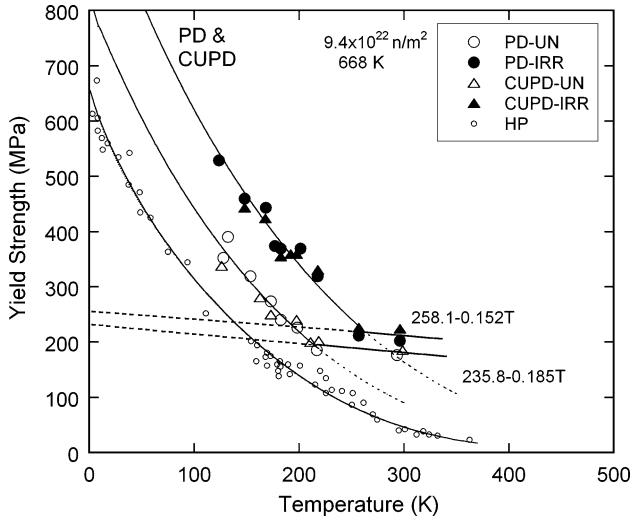

Fig. 5—Temperature dependence of yield strength (σ_y) for UN and IRR P-doped and Cu-P-doped alloys, compared with that of HP iron. The data are fitted to rate equations representing linear and nonlinear curves.

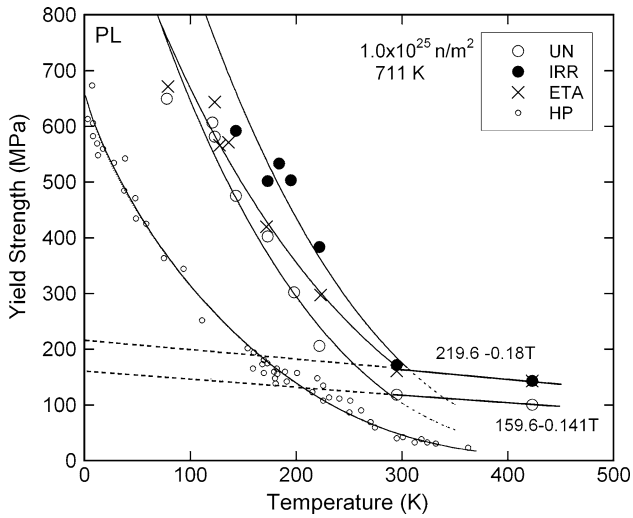

Fig. 6—Temperature dependence of yield strength (σ_y) for UN, IRR, and ETA low P-doped alloys, compared with that of HP iron. The data are fitted to rate equations representing linear and nonlinear curves.

The temperature dependence of the yield stress for the various unirradiated, irradiated, and aged impurity-doped ferritic alloys are shown in Figures 4 through 10, compared with the data of unirradiated high-purity iron obtained by Matsui *et al.*[25] In a temperature range between 215 and 330 K, the yield strength rapidly increases, due to the transition from DO- to LR-controlled plasticity. Neutron irradiation or thermal aging shifts the transition temperature (T_c) to higher temperature only when unirradiated alloys such as CUD, PD, CUPD, and PM have a lower T_c of 215 to 240 K (Table III). High-purity iron tested above 300 K shows very low yield stress and, therefore, negligible DO-controlled plasticity. In order to estimate the athermal and activation energy representing the two

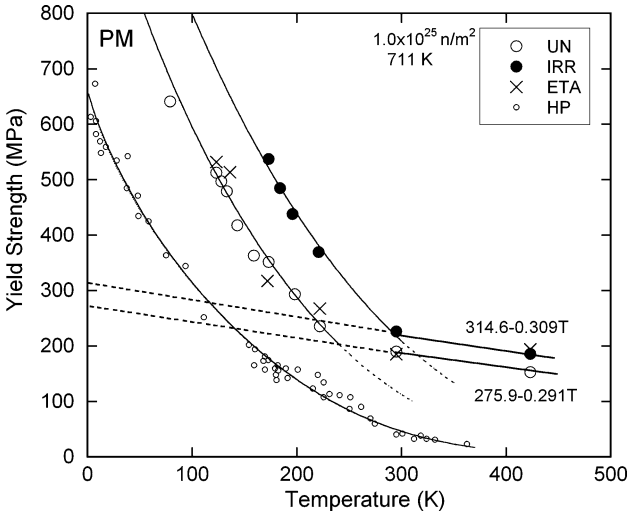

Fig. 7—Temperature dependence of yield strength (σ_y) for UN, IRR, and ETA moderately P-doped alloys, compared with that of HP iron. The data are fitted to rate equations representing linear and nonlinear curves.

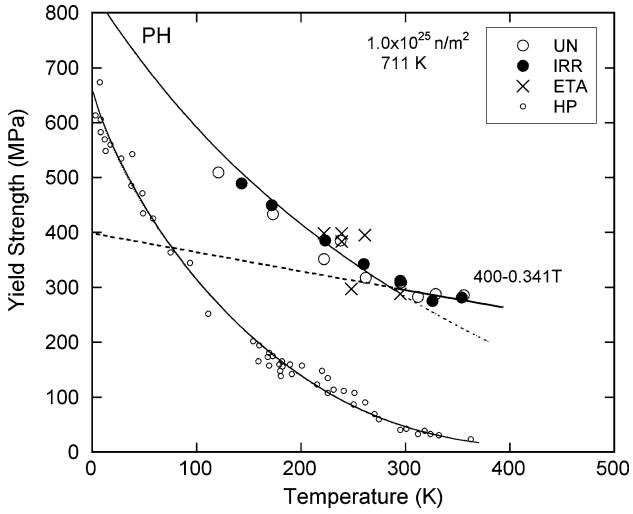

Fig. 8—Temperature dependence of yield strength (σ_y) for UN, IRR, and ETA highly P-doped alloys, compared with that of HP iron. The data are fitted to rate equations representing linear and nonlinear curves.

differing plasticity mechanisms, the dependence of the yield stress on temperature is fitted using least-squares and regression to Eqs. [3] and [5] above and below T_c, respectively. The fitted curves are plotted, along with the experimental data, in Figures 4 through 10. The athermal stress and activation energy empirically determined for DO- and LR-controlled plasticity are listed in Table III for the various unirradiated, irradiated, and thermally aged ferritic alloys.*

*DO-controlled hardening has usually been characterized by the yield strength at room temperature ($(\sigma_y)_{RT}$). Two linear relationships between the σ_a^o and $(\sigma_y)_{RT}$ were found, depending on the activation energy. The $(\sigma_y)_{RT}$ is 75 pct of the σ_a^o in the group I and II alloys with ΔF^o below ~600 kJ/mole and 87 pct of the σ_a^o in the group III alloys irradiated below 563 K, with ΔF^o above ~800 kJ/mole.

Several characteristics of plasticity and problems of data analysis and acquisition are pointed out in the impurity-doped alloys as follows: (1) this study focuses on slip deformation mechanisms, therefore excluding the yield stress controlled by mechanical twining associated with serration, load drop, audible noise or brittle intergranular cracking at very low temperatures; (2) neutron irradiation and ETA at 711 K produce the same hardening behavior in the PL and PM alloys, so that the hardening is controlled by thermal annealing and not irradiation (Figures 6 and 7); (3) the addition of copper or nickel does not affect the σ_y in unirradiated P-doped alloys (Figures 5 and 10); (4) discrete obstacle-controlled plasticity in irradiated CUD alloys is analyzed by assuming the same temperature dependence of the σ_y as that in the unirradiated alloys, due to the lack of data above room temperature (RT); and (5) the $(\sigma_y)_{RT}$ of MA, MCu, and MNi alloys irradiated at 473 K is estimated from the hardness measurement, and reliable data of the σ_y cannot be obtained below 300 K because of severe intergranular embrittlement (Figure 10).[13]

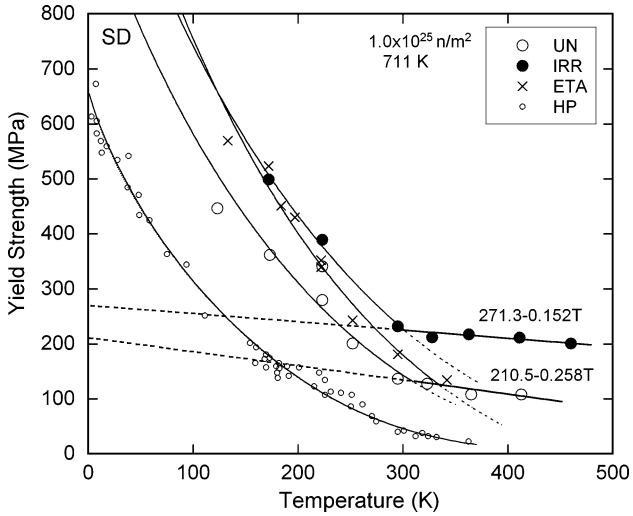

Fig. 9—Temperature dependence of yield strength (σ_y) for UN, IRR, and ETA S-doped alloys, compared with that of HP iron. The data are fitted to rate equations representing linear and nonlinear curves.

B. *Discrete Obstacle-Controlled Plasticity*

Increasing the thermal energy above T_c assists dislocations growing under a high-energy barrier of solute or precipitate. The values of σ_a^o for the varying impurity-doped alloys are plotted against $\sqrt{C_P}$, $\sqrt{C_S}$, and $\sqrt{C_{Cu}}$ in Figure 11. In all unirradiated and irradiated P-doped alloys except group III (MA, MCu, and MNi) alloys irradiated below 563 K, the athermal stress is proportionately related to the square root of the P content. The difference in the σ_a^o between the unirradiated and irradiated or aged P-doped alloys diminishes with increasing P content. In unirradiated alloys, the addition of Cu does not increase the value of σ_a^o much, compared with an alloy with similar P contents (PM alloy). The athermal stress of

the unirradiated and aged S-doped alloys is similar to that of the irradiated PL alloy.

In order to demonstrate irradiation hardening controlled by discrete obstacles, the increased values of athermal stress ($\Delta\sigma_a^o$) by neutron irradiation are plotted against the neutron irradiation temperature in Figure 12.

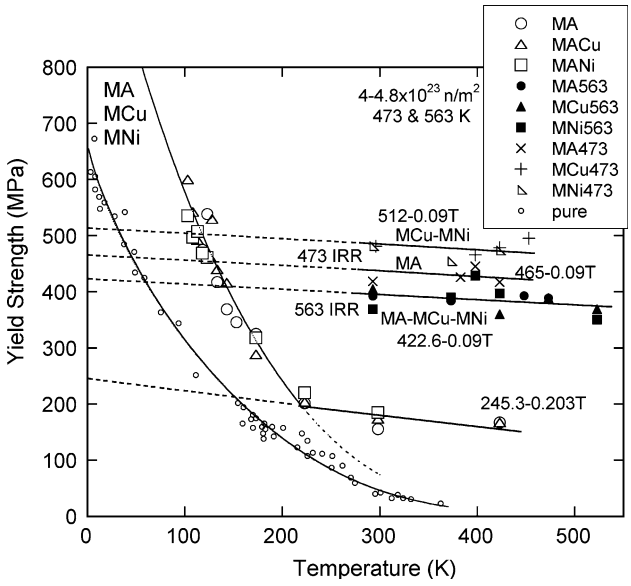

Fig. 10—Temperature dependence of yield strength (σ_y) for UN and IRR Mn-P-doped, Mn-P-Cu-doped, and Mn-P-Ni-doped alloys, compared with that of HP iron. The data are fitted to rate equations representing linear and nonlinear curves.

In this figure, the $\Delta\sigma_a^o$ is regarded as zero for the P-doped group II alloys, because of the thermal hardening, as mentioned earlier, and it represents the data for the bulk content of $C_P \sim 0.067$ at. pct, $C_{Cu} \sim 0.25$ at. pct, and $C_S \sim 0.016$ at. pct. Phosphorus-doped (MA, MCu, and MNi) alloys neutron irradiated below 563 K depict much larger hardening than do PD-CUPD alloys irradiated at 668 K. Since high-temperature irradiation under the high and low fluence evidently causes negligible and

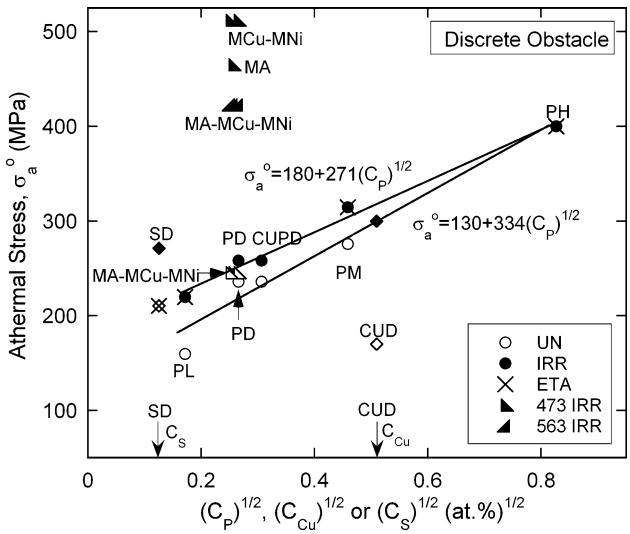

Fig. 11—Variation of DO-controlled athermal stress (σ_a^o) with $\sqrt{C_P}$, $\sqrt{C_{Cu}}$, or $\sqrt{C_S}$ (at. pct)$^{1/2}$, in varying UN, IRR, and ETA alloys.

Table III. Summary of T_c, Activation Energy, and Athermal Stress for DO- and LR-Controlled Plasticity in Various UN, IRR, and ETA Alloys, Together with Irradiation and Thermal Aging Conditions; Subscript of Bulk Content (C_i): i = P, for All P-doped Alloys, i = Cu, for CUD Alloy, and i = S, for SD Alloy

Group	IRR or EAT	Alloys	$\sqrt{C_i}$ (√at. pct)	Type	T_c (K)	DO: σ_a^0 (MPa)	DO: ΔF^0 (kJ/mole)	LR: σ_a^l (MPa)	LR: ΔF^l (kJ/mole)
—	—	HP Fe	—	UN	—	—	—	671.4	56.1
I	9.4×10^{22}	CUD	0.51	UN	223.5	170	146	1027	44.1
	668 K 127 h			IRR	262.8	300	258	1238.8	66.1
		PD-CUPD	0.266	UN	213.7	235.8	203	888.9	53.4
			0.307	IRR	260.8	258.1	271	1153.2	62.5
II	1.0×10^{25}	PL	0.172	UN	291	159.6	189	1364.1	54.2
	711 K 2120 h			IRR	300	219.6	204	1751.8	60.5
				ETA	291	219.6	204	1268.3	63.6
		PM	0.459	UN	239.2	275.9	158	1208	56.8
				IRR	290.2	314.6	169	1481	67.3
				ETA	239.2	314.6	169	1208	56.8
		PH	0.827	UN	286.3	400	196	891.6	102.1
				IRR	286.3	400	196	891.6	102.1
				ETA	286.3	400	196	891.6	102.1
		SD	0.126	UN	307.8	210.5	136	1099	63.2
				IRR	300	271.3	298	1310.2	72.7
				ETA	333.3	210.5	136	1433.2	64.3
III	4×10^{23}	MA	0.256	UN	215.5	245.3	202	1289.9	50.0
	473 K 1067 h			IRR 473	< 300	465	897	—	—
				IRR 563	< 300	422.6	815	—	—
	4.8×10^{23}	MCu	0.265	IRR 473	< 300	512	987	—	—
	563 K 1178 h			IRR 563	< 300	422.6	815	—	—
		MNi	0.252	IRR 473	< 300	512	987	—	—
				IRR 563	< 300	422.6	815	—	—

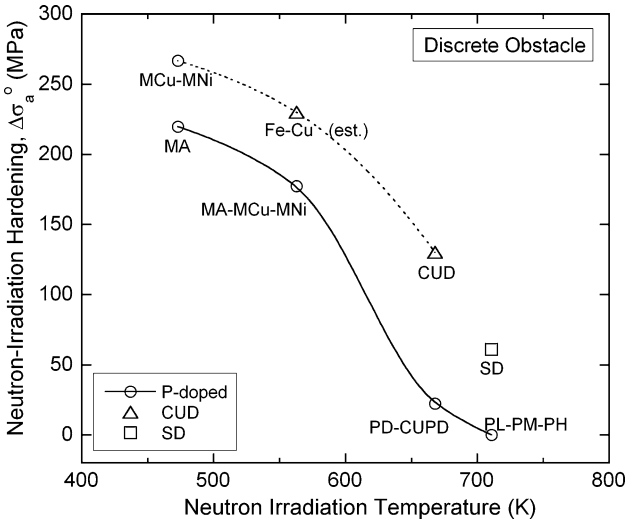

Fig. 12—Effect of neutron irradiation temperature on DO-controlled hardening ($\Delta\sigma_a^o$) in various impurity-doped alloys.

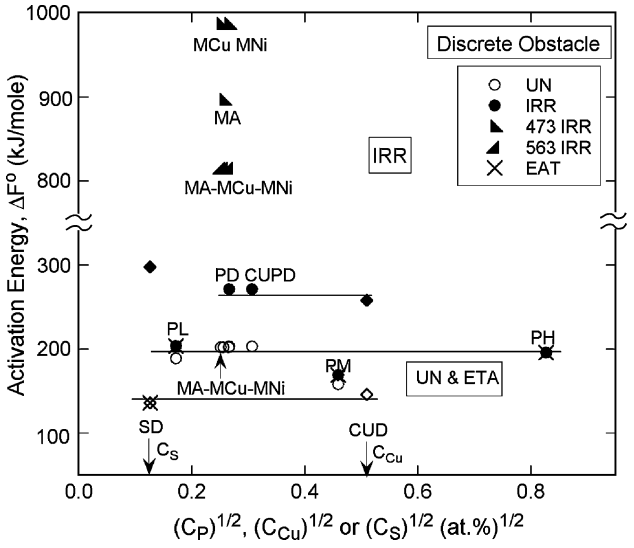

Fig. 13—Variation of DO-controlled activation energy (ΔF^o) with $\sqrt{C_P}$, $\sqrt{C_{Cu}}$ or $\sqrt{C_S}$ (at. pct)$^{1/2}$, in UN, IRR, and ETA alloys.

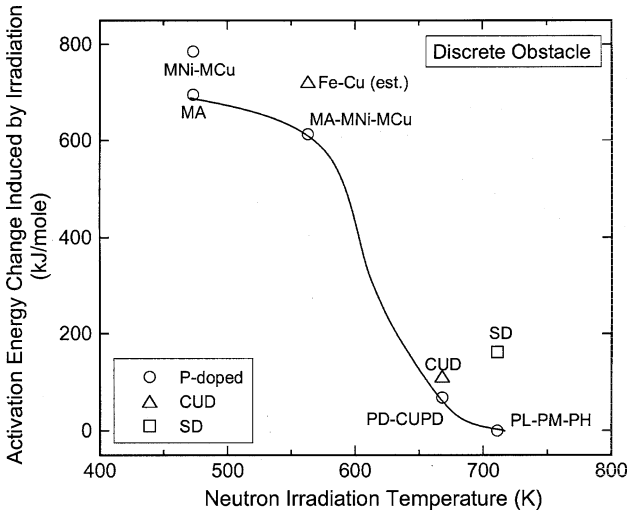

Fig. 14—Effect of irradiation temperature on increased activation energy for DO-controlled plasticity in various ferritic alloys.

weak hardening (Figures 3 and 12), decreasing the neutron irradiation temperature becomes a key factor controlling hardening; it is a more significant factor than increasing the fluence. This is consistent with the lack of dependence of the irradiation hardening of Fe-Cu alloys on fluence above 1×10^{22} n/m^2.[29] Adding copper or nickel in P-doped alloys enhances hardening under neutron irradiation at 473 but not at 563 K. The dependence of the athermal stress on the irradiation temperature in Cu-bearing alloys, which is partly estimated from the $(\sigma_y)_{RT}$ in a Fe-0.25 at. pct Cu alloy irradiated at 563 K,[20] is upwardly shifted from that in the P-doped alloys. Weak irradiation hardening observed in an S-doped alloy irradiated at 711 K tends to fall into the curve extrapolated from the results in the Cu-bearing alloys.

In Figure 13, the relationship of the activation energy to the square root of the impurity content is indicated for the impurity-doped alloys. Unlike the σ_a^o, the ΔF^o of the unirradiated P-doped alloys remains almost the same (about 200 kJ/mole), independent of the P content. The unirradiated CUD and SD alloys have a slightly lower ΔF^o, at 140 kJ/mole. The P-doped group III (MA, MCu, and MNi) alloys irradiated below 563 K have high values of ΔF^o, between 815 and 987 kJ/mole. Neutron irradiation at 668 K raises the activation energy of the PD-CUPD alloys to ~265 kJ/mole, but no effect of irradiation at 711 K is observed in the P-doped group II (PL, PM, and PH) alloys. The variation in the increased ΔF^o by the irradiation to the irradiation temperature is similar to that of the $\Delta\sigma_a^o$ (compare Figures 14 and 12). That is, both the parameters are proportionally correlated with each other regardless of the irradiation conditions in all the alloys, with the exception of the CUD alloy. It is evident that the irradiation effect on the ΔF^o in the CUD alloy would have been underestimated by assuming the same proportionality constant of temperature dependence of the yield stress, despite the decreased proportionality in irradiated alloys, as in Figures 5, 9, and 10.

The increased ΔF^o in the Cu-doped alloy neutron irradiated at 563 K,[20] estimated using the linear relation between the increased σ_a^o and ΔF^o, is compared with that in the P-doped alloy in Figure 14.

C. *Lattice Resistance-Controlled Plasticity*

The dislocation motion produced by overcoming the lattice resistance that dominates below T_c is controlled by the nucleation of kink pairs.[15–17,30] Plasticity that is LR-controlled requires a larger athermal stress and a smaller activation energy than does DO-controlled plasticity. The variations in the σ_a^l and ΔF^l with $\sqrt{C_P}$, $\sqrt{C_S}$, and $\sqrt{C_{Cu}}$ are indicated in Figures 15 and 16. All the impurity-doped alloys show higher athermal stress than does the unirradiated high-purity iron (Figure 15). High-temperature (above 668 K) neutron irradiation

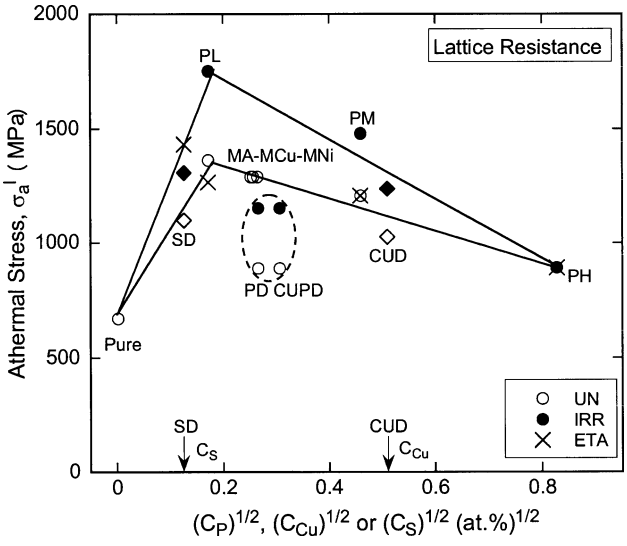

Fig. 15—Variation of LR-controlled athermal stress (σ_a^l) with $\sqrt{C_P}$, $\sqrt{C_{Cu}}$, or $\sqrt{C_S}$ (at. pct)$^{1/2}$, in varying UN, IRR, and ETA alloys.

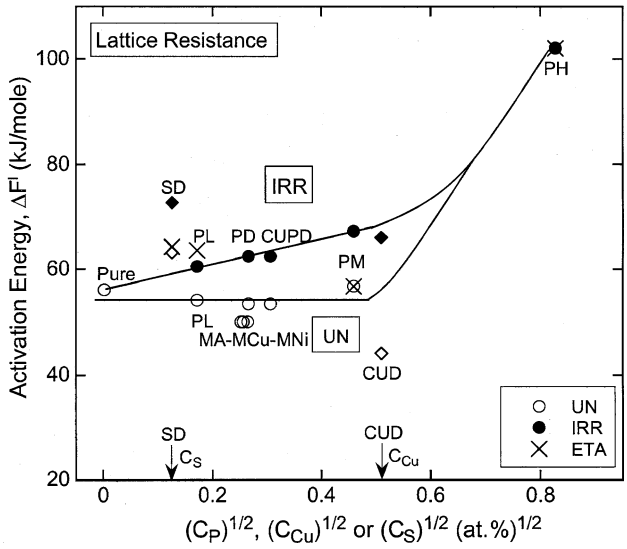

Fig. 16—Variation of LR-controlled activation energy (ΔF^l) with $\sqrt{C_P}$, $\sqrt{C_{Cu}}$, or $\sqrt{C_S}$ (at. pct)$^{1/2}$, in varying UN, IRR, and ETA alloys.

causes LR-controlled hardening in alloys with a low to moderate content of impurities, although the thermal ageing does not affect the plasticity. This is in marked contrast with the negligible or small effect of neutron irradiation above 668 K on DO-controlled plasticity. As the P content is increased, the athermal stress of the irradiated alloys decreases more rapidly than that of the unirradiated alloys, and both converge with each other when C_i = 0.68 at. pct. The data of the unirradiated and irradiated CUD alloys lie along the curves of all the P-dpoed alloys, except for the PD-CUPD alloys; this indicates lower σ_a^l values, as marked by a broken circle. The disagreement of the unirradiated and irradiated PD and CUPD alloys with the other alloys might be related to the small content of interstitial impurities affecting weakly the σ_a^l but not the σ_a^o. Taking into account the results of the SD alloy and high-purity iron together with those of most of the P-doped alloys, the σ_a^l of both the unirradiated and irradiated alloys with $C_i \cong 0.03$ at. pct shows a peak regardless of the type of impurities.

As shown in Figure 16, the unirradiated high-purity iron and many P-doped alloys except the PH alloy have a low activation energy (~54 kJ/mole), which is in fair agreement with the nucleation energy of kink pairs.[15–17] However, the PH alloy has a high activation energy of ~100 kJ/mole, which would be reflected by the growth of kink pairs independent of the thermal treatment and irradiation. The addition of copper and sulfur in unirradiated alloys lead to a reduction and increase in the ΔF^l, respectively. The effect of neutron irradiation on the activation energy slightly rises with increased P content, except in the PH alloy. Neutron irradiation at 668 K exerts the largest effect on the ΔF^l in the CUD alloy because the CUD alloy has the lowest ΔF^l among the unirradiated alloys. The activation energy of the SD alloy irradiated at 711 K exceeds that of most of the other alloys.

IV. MECHANISMS CONTROLLING NEUTRON IRRADIATION HARDENING

A. *Solid Solution and Precipitation Hardening*

In an effort to gain a fundamental knowledge of the irradiation hardening mechanism, it is important to analyze how the phase transformation from solid solution to precipitation influences DO-controlled hardening in the impurity-doped alloys. Based on the solubility limit of impurities, which decreases for S, Cu, and P, in that order,[31–33] all the P-doped alloys except the PH and Cu-doped alloys maintain solid solution during the thermal annealing and ETA. However, sulfide (FeS) precipitates are dispersed in the thermally treated and irradiated S-doped alloy (Table IV), thereby indicating a higher σ_a^o than in the unirradiated CUD and PL alloys (Figure 11). The effects of P and Cu on DO-controlled hardening are compared using the $(\sigma_y)_{RT}$ instead of the σ_a^i, which is not measured in most studies on the Cu effect.[18–20]

Phosphorus and copper produce solid solution hardening in unirradiated ferritic alloys. According to Eq. [AI-10a] in Appendix I, the $\Delta\sigma_y^s$ values are plotted against $\sqrt{C_P}$ and $\sqrt{C_{Cu}}$, (atomic fraction)$^{1/2}$, in Figure 17, which are determined by subtracting the $(\sigma_y)_{RT}$ of the high-purity iron from that of the unirradiated P-doped and CUD alloys and solution-treated Fe-Cu alloys.[18,20] The copper-solution hardening values of the two types of alloys agree well. Phosphorus causes a solution hardening larger by 1.8 times than that of copper, when C_{Cu} is less than 1.44 at. pct. This result is consistent with the slightly higher activation energy observed in the unirradiated P-doped alloys (Figure 13).

Neutron irradiation hardening mainly occurs due to precipitation arising from the dynamic interaction between defects and impurities in impure alloys. Despite nonequilibrium microstructural evolution during neutron irradiation, it is possible that irradiation-induced

Table IV. Estimate of Solid Solution and Precipitation in UN, IRR, and ETA Impurity-Doped Alloys or A533 B Steel

Alloys and Steel (Wt Pct)	UN (873 K for 1 to 2 h)	ETA (668 K for 127 h)	ETA (711 K for 2120 h)	ETA (473 and 563 K for 1067 and 1179 h)	IRR (473 to 711 K)
PL, PM, PD, PH (P < 0.38)	solid solution	solid solution	solid solution or precipitation	—	—
MA (P = 0.036)	solid solution	—	—	solid solution	precipitation: Fe_3P
CUD (Cu = 0.29) Fe-Cu	solid solution	solid solution	—	solid solution	precipitation: pure Cu
SD (S = 0.009)	solid solution or precipitation	—	precipitation: FeS	—	precipitation: FeS
A533B	precipitation: carbide	—	—	—	precipitation: Fe-Cu-(MnNiSi)

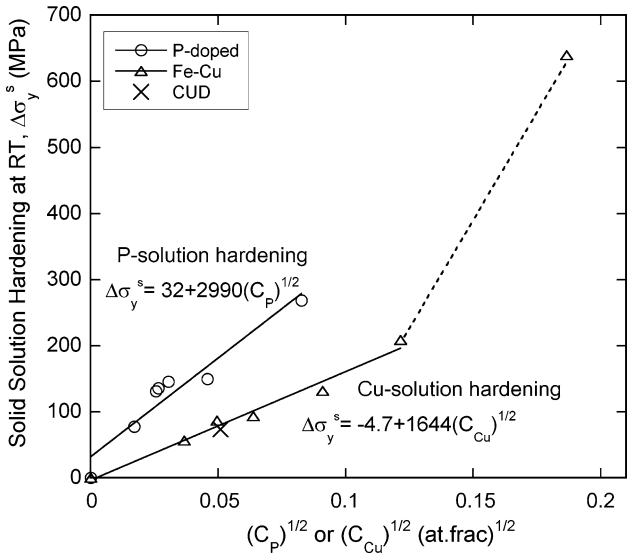

Fig. 17—Dependence of P- and Cu-solution hardening ($\Delta\sigma_y^s$) at RT on $\sqrt{C_P}$ and $\sqrt{C_{Cu}}$ (at. frac.)$^{1/2}$. The data of Fe-Cu alloys obtained in Refs. 18 and 19 are plotted.

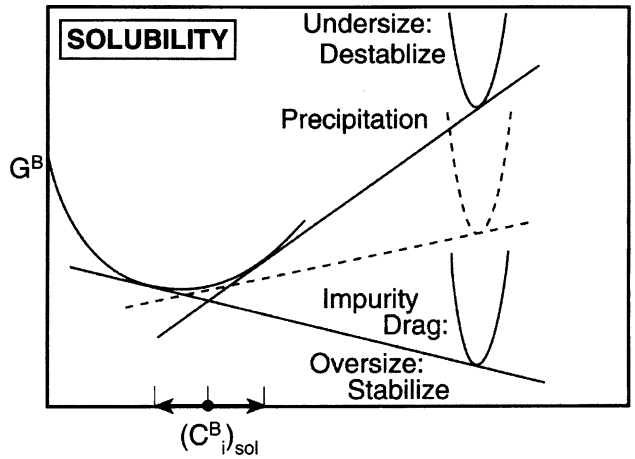

Fig. 18—Schematic representation of change in hypothetical free energy of precipitates induced by neutron irradiation, leading to solubility change.

precipitation is interpreted in terms of the hypothetical free energy, which controls the stability of precipitates in Figure 18. Maydet and Russell[34] have demonstrated that in irradiated materials, undersized incoherent precipitates, where outward fluxes of vacancies are developed, are destabilized by increasing the free energy, while inward vacancy fluxes stabilize oversized precipitates. Thus, it is suggested that the impurity drag, associated with the vacancy inward flux, causes the stabilization of precipitates regardless of size by decreasing the free energy of the precipitate. This thermodynamic argument is supported by the recent results of molecular dynamics simulation analysis.[9] Additionally, neutron irradiation accelerates the kinetics of precipitation, which gradually proceeds under the thermal condition at lower temperatures than 563 K.[35]

Decreasing the neutron irradiation temperature facilitates impurity-rich precipitation not associated with the coarsening, due to the impurity-vacancy drag effect, and gives rise to an increase in the σ_a^o and ΔF^o. The dislocation pinning strength of the precipitate, which is related to the activation energy for DO-controlled plasticity, can be determined by the relationship of hardening ($\Delta\sigma_y^p$) to a product of the ratio of the magnitude of the Burgers vector (**b**) to the precipitate size and the square root of volume fraction of precipitate ($(\mathbf{b}/d)\sqrt{f_v}$), indicating a $\kappa_p\varphi\mu$ term of Eq. [AI-10b] in Appendix I. When dislocations grow by cutting precipitates, the pinning strength increases when the elastic modulus of the precipitate is reduced relative to the matrix[17,18] and the particle size is increased.[36,37]

The SANS analysis indicates that the volume fraction of precipitates (identified as ferromagnetic Fe_3P) are 0.032 and 0.026 in MA alloys irradiated at 473 and 563 K, respectively, and the precipitate size remains the same at ~1.7 nm. On the other hand, A533B steel and Fe-Cu alloys irradiated at 563 K or peak aged at 748 to 798 K[3,18–20] have exhibited differing precipitates of (80 to 68)Fe-11Cu-(9 to 21)(MnNiSi) and pure Cu with precipitate sizes of ~2.5 and 2.1 nm, larger than the Fe_3P (Table IV). To compare the pinning strength of the various precipitates, the values of $\Delta\sigma_y^p$ for the irradiated MA alloys, the A533B steel, and the peak-aged or irradiated Fe-Cu alloys containing Cu less than 1.6 wt pct are correlated to $(\mathbf{b}/d)\sqrt{f_v}$ of the Fe_3P, Fe-Cu-(MnNiSi), and pure Cu precipitate, respectively, in Figure 19. In this figure, there are three features: (1) $\Delta\sigma_y^p = 0$ is plotted when the f_v of Fe_3P and Fe-Cu-(MnNiSi) precipitates measured by SANS is zero; (2) the

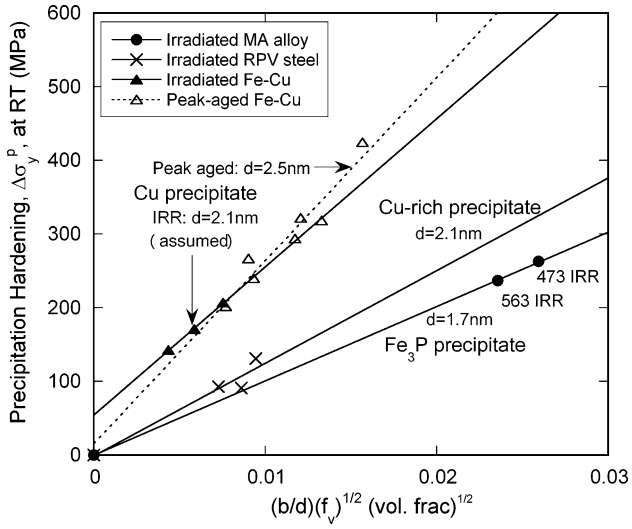

Fig. 19—Dependence of precipitation hardening ($\Delta\sigma_y^p$) at RT on $(b/d)\sqrt{f_v}$ of Fe_3P, pure Cu, and Cu-rich precipitates.

f_v value of the peak-aged and irradiated Fe-Cu alloys means the bulk atom fraction of Cu[18–20] and the peak-aging hardening[18] is corrected by analyzing properly the data of Fujii *et al.*;[19] (3) the precipitate size of the irradiated Fe-Cu alloy[20] is assumed to be 2.1 nm. In Figure 20, the pinning strength represented by the slope of Figure 19 is plotted against the logarithmic precipitate size, according to Eq. [AI-11b][36,37] and the size dependence of pinning strength in the irradiated Fe-Cu alloy is also shown. As a result of similar stiffness (the modulus ratio to the matrix is ~0.95) in the Fe_3P and Fe-Cu-(MnNiSi) precipitates,[38] the difference in their pinning strength is due to the size effect. The large pinning strength of the Cu precipitate is ascribed to the low modulus of copper relative to iron[18] and the Cu precipitate has a slightly stronger size effect than the

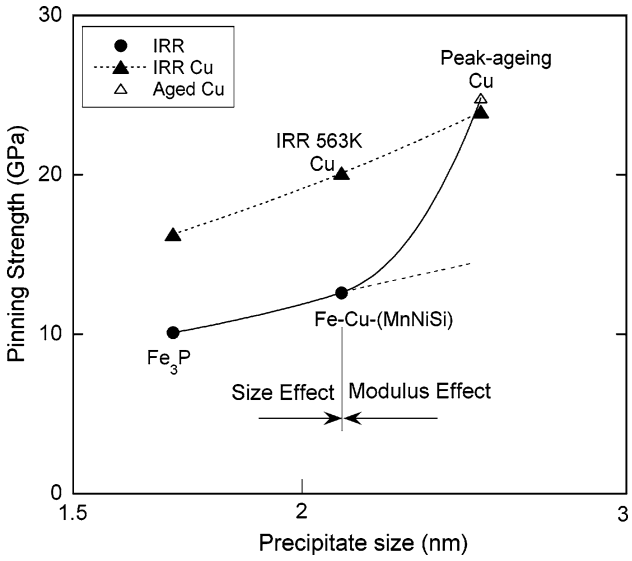

Fig. 20—Variation of pinning strength to logarithmic size of Fe_3P, Cu-rich, and pure Cu precipitates for IRR P-doped alloys, A533B steel and peak-aged or IRR Cu-doped iron.

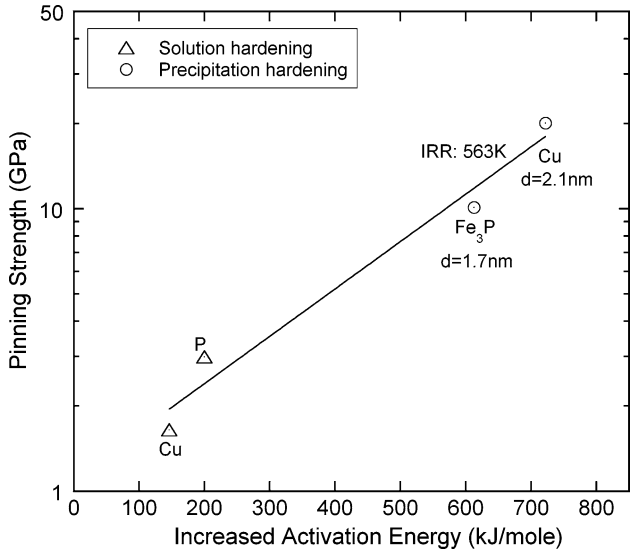

Fig. 21—Exponential dependence of pinning strength on increased activation energy for solid solution and precipitation hardening.

Cu-rich or Fe_3P ones. As indicated in Figure 21, it is interesting to see that the pinning strength of different types of precipitate and solute exponentially rises with the increased activation energy.

Another issue to be pointed out is that the formation of defect clusters plays a key role in the irradiation hardening of high-purity alloys. Despite no available data for irradiated high-purity alloys, it is possible to examine the activation energy required for dislocation motion through the defect cluster in irradiated high-purity A533B steel with quenched and tempered microstructure.[39] The complex microstructure with and without the defect clustering possesses the same ΔF^o of ~380 kJ/mole, so that the increased density in dislocation pinning sites is responsible for the irradiation hardening. Because of activation energy in the irradiated high-purity steel that is lower than that in the P-doped alloys irradiated below 563 K, the matrix damage does not become a controlling factor for DO-controlled irradiation hardening in the impure alloys.

B. *Effects of Impurity and Neutron Irradiation on Formation of Kink Pairs*

Below T_c, a reduction in the thermal energy makes the generation of kink pairs more difficult than the growth, thereby requiring high flow stress. Increasing the amount of dissolved impurities, which would act as nucleation sites of kink pairs, exerts a complicated effect on LR-controlled plasticity, and high-temperature irradiation impedes the kink-pair formation, depending on the content of impurities (Figures 15 and 16).[40] Two competitive effects on the nucleation of kink pairs bring about the maximization of the athermal stress, when $C_i \cong 0.03$ at. pct. The athermal stress initially would rise with an increasing amount of dissolved substitutional impurities, due to the narrowing of the spacing of kink nucleation sites. Conversely, further increasing the impurity content that raises the density of nucleated

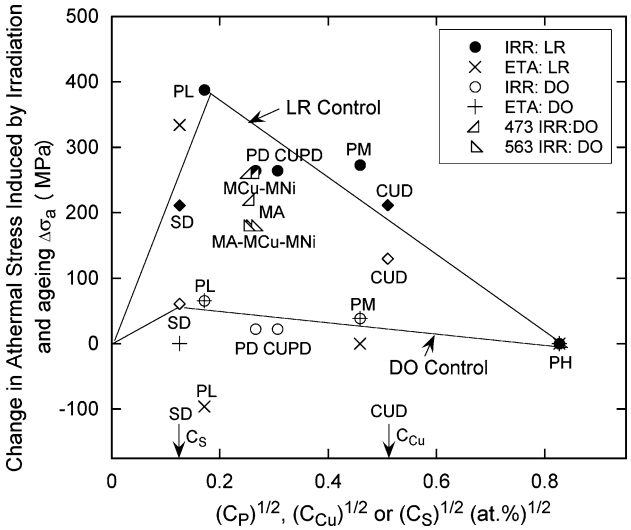

Fig. 22—Variation in changes in LR- and DO-controlled athermal stresses ($\Delta\sigma_a^o$ and $\Delta\sigma_a^l$) caused by neutron irradiation and ETA with $\sqrt{C_P}$, $\sqrt{C_{Cu}}$ or $\sqrt{C_S}$ (at. pct)$^{1/2}$, in varying impurity-doped alloys.

kink pairs would allow kink pairs to easily spread apart by combining with neighboring kink pairs, therefore reducing the σ_a^l. Because of the strong interaction between densely nucleated kink pairs, the plasticity of the PH alloy is not affected by the neutron irradiation and ETA, but is controlled by the growth of kink pairs with a high activation energy of 100 kJ/mole. As a result of increasing the formation energy of kink pairs (Figure 16), irradiation hardening ($\Delta\sigma_a^l$) becomes more significant in a low-to-medium range of the impurity content (Figure 22). It is noted that the $\Delta\sigma_a^l$ of the PD-CUPD alloys roughly falls into the curve of the other alloys by offsetting the effect of interstitial impurities on the σ_a^l, which would not be influenced by the irradiation. Moreover, precipitation hardening in the MCu and MNi alloys irradiated at 473 K becomes comparable to LR-controlled hardening under high-temperature irradiation.

C. *Precipitation and Intergranular Segregation during Neutron Irradiation*

We finally attempt to discuss a deferring role of dynamic interaction between impurities and defects in neutron-irradiation-induced precipitation and intergranular segregation. Guttmann and McLean[41] have suggested that the precipitation and grain-boundary segregation of impurities are analogous phenomena. Thus, lowering the aging temperature enhances the impurity precipitation and equilibrium segregation by decreasing the solubility limit of impurities. However, our recent study[13] has shown that intergranular phosphorus segregation is promoted by raising the irradiation temperature to 668 K, as opposed to the irradiation hardening. The addition of metallic elements such as copper or nickel mitigates irradiation-induced P segregation, while it facilitates the irradiation hardening. These observations are indicative of the competition between precipitation and segregation, and of the different interaction of dissolved phosphorus with defects in the grain matrix and near the grain boundaries. Based on a post-irradiation annealing (PIA) study on the group I alloys,[35] the intergranular segregation of P and S proceeds as a result of the rapid diffusion during the early stage of PIA at temperatures lower than the irradiation temperature of 668 K. The low activation energy estimated for the rapid diffusion of P and S suggests that P-interstitial complexes would assist the P segregation and that lowering the formation energy of vacancies would promote the vacancy exchange mechanism controlling S diffusion. An intriguing implication of the PIA study is that interstitials and vacancies interacting with P and S could survive during PIA at higher temperatures for a longer time than expected for annihilation of point defects not interacting with impurities.

The fast diffusion of impurities, occurring even during low-temperature irradiation, is not necessarily a controlling factor in neutron-irradiation-induced segregation. Instead, the segregation energy of grain boundaries, which act as a defect sink, controls the nonequilibrium impurity segregation, On the basis of first-principle calculations on intergranular segregation of P and S in iron,[42] the segregation energy of the metalloid impurities decreases with increasing amount of segregants, due to the repulsive interaction of the segregants at grain boundaries. This is contrary to McLean's theory of equilibrium segregation, which assumes that the constant segregation energy is independent of the amount of segregants and the aging temperature.[43] Therefore, it is expected that, under neutron irradiation, the annihilating flux of vacancies would raise the capacity of grain boundaries to absorb segregants by suppressing the repulsive interaction of segregated impurities. The higher the irradiation temperature, the larger the annihilating fluxes of vacancies that are developed into grain boundaries. Consequently, high-temperature neutron irradiation promotes nonequilibrium impurity segregation. This is the opposite of the precipitation behavior in irradiated alloys, which becomes more stabilized as the irradiation temperature is decreased.

V. CONCLUSIONS

By applying a rate theory to the temperature dependence of the yield strength, hardening mechanisms under neutron irradiation at various temperatures (473 to 711 K) in a variety of impurity-doped ferritic alloys have been studied in light of the dynamic interaction of precipitated and dissolved impurities with the nucleation and growth of dislocations.

1. Hardening behavior induced during neutron irradiation is investigated in terms of the variations in the athermal stress and activation energy for DO- and LR-controlled plasticity, with the content of substitutional impurities such as P, Cu, and S.
2. In unirradiated alloys, the addition of P more appreciably causes solid solution hardening than the addition of Cu, and the weaker effect of the Cu

solution is related to the lower formation energy of kink pairs.
3. Neutron irradiation below 563 K causes a drastic increase in the athermal stress and activation energy for precipitation-controlled plasticity in P-doped alloys. During high-temperature (above 668 K) irradiation, precipitation hardening occurs to a limited extent in Cu-doped and S-doped alloys, compared to small or negligible hardening in the P-doped alloys.
4. The SANS analysis of P-doped alloys has indicated that the volume fraction of P-rich precipitates increases with decreasing irradiation temperature, but the precipitate size remains the same (smaller than the Cu and Cu-rich precipitates in irradiated alloys reported by other works).
5. Comparison of the present results with other investigations indicates that the P-rich precipitate has a lower dislocation-pinning strength, which more weakly depends on the size, compared to Cu precipitates with strong modulus effects. The pinning strength of the various precipitations and solutes exponentially increases with the increased activation energy.
6. Under neutron irradiation above 668 K, hardening controlled by kink-pair formation, associated with a small increase in the activation energy, is observed in alloys with a low-to-moderate content of impurities.
7. The inverse effects of neutron irradiation temperature on hardening and intergranular P segregation observed in our recent study are discussed in light of the different dynamic interactions of dissolved impurities with defects in the grain interior and near-grain boundaries.

ACKNOWLEDGMENTS

This research was partly supported by the United States Department of Energy, the Office of Basic Energy Sciences, Division of Materials Sciences and Engineering, while one of the authors (JK) was affiliated with Ames Laboratory operated by Iowa State University under Contract No. W-7405-ENG-82. The authors also acknowledge the support of the National Institute of Standard and Technology, United States Department of Commerce, in providing the neutron research facilities used in this experiment.

APPENDIX I

Rate theory

A fundamental principle of rate controlling theory is that the shear strain rate ($d\gamma/dt$) is proportionally related to the average velocity of dislocations (V) and the density of mobile dislocations (ρ_m):[15]

$$d\gamma/dt = \rho_m \mathbf{b} V \qquad [\text{AI} - 1]$$

where **b** is the magnitude of the Burgers vector. Under steady state, the value of ρ_m parabolically increases with increasing shear flow stress (τ_s); *i.e.*,

$$\rho_m = \alpha(\tau_s/\mu\mathbf{b})^2 \qquad [\text{AI} - 2]$$

where μ is the shear elastic modulus and α is a dimensionless constant. The dislocation mobility is thermally activated under the shear flow stress and is appreciably changed depending on two types of barriers, such as discrete obstacles and lattice resistance. The rate of dislocation motion can be described in terms of the Gibbs free energy ($\Delta G(\tau_s)$) that depends on the flow stress

$$V = \beta \mathbf{b} v \exp\left[-\Delta G(\tau_s)/\mathrm{R}T\right] \qquad [\text{AI} - 3]$$

where β is a dimensionless constant, R is the gas constant, ν is the Debye frequency, and T is the absolute temperature. The magnitude of activation energy is related to how the nucleation and growth of dislocations are influenced by discrete obstacles such as solute atoms, precipitates, and forest dislocations, and by lattice resistance. Although the activation area is theoretically introduced to describe the effect of flow stress, the Gibbs free energy is phenomenologically described in Eq. [AI-4], because of ambiguous physical meanings of the activation area indicating the temperature dependence:[15,16]

$$\Delta G(\tau_s) = \Delta F^i \left\{1 - \left(\tau_s/\tau_a^i\right)^p\right\}^q \qquad [\text{AI} - 4]$$

where ΔF^i is the Hermholtz free energy not influenced by the stress; τ_a^i is the athermal shear stress at 0 K; p and q are empirical factors that would depend on the shape of dislocation barriers and the superscript of the activation energy and athermal stress; and subscript $i = o$ and l, for DO- and LR-controlled plasticity. Using Eqs. [AI-1] through [AI-4], the rate equation for the dislocation motion is given by

$$d\gamma/dt = \alpha\beta\nu(\tau_s/\mu)^2 \exp\left[-\left(\Delta F^i/\mathrm{R}T\right)\left\{1 - \left(\tau_s/\tau_a^i\right)^p\right\}^q\right] \qquad [\text{AI} - 5]$$

In the case of the DO-controlled glide, $(\tau_s/\mu)^2$, p and q can be unity because of the large value of ΔF^o. The pre-exponential term [$(d\gamma/dt)_o$, $= \alpha\beta\nu$] is empirically given by $10^6\ \mathrm{s}^{-1}$. Converting the shear flow stress and strain components into the tensile yield stress (σ_y) with $\sigma_y = \sqrt{3}\tau_s$ and $\varepsilon = \gamma/\sqrt{3}$, the rate equation for DO-controlled plasticity using the tensile stress and strain components is given by

$$d\varepsilon/dt = \left\{10^6/\sqrt{3}\right\}\exp\left[-(\Delta F^o/\mathrm{R}T)\left\{1 - \left(\sigma_y/\sigma_a^o\right)\right\}\right] \qquad [\text{AI} - 6]$$

For LR-controlled plasticity with low ΔF^l, $p = 3/4$, $q = 4/3$, and $(d\gamma/dt)_o = 10^{11}\ \mathrm{s}^{-1}$ are experimentally used, and the rate equation is

$$d\varepsilon/dt = \left\{\left(10^{11}/3\sqrt{3}\right)\right\}\left(\sigma_y/\mu\right)^2 \exp\left[-\left(\Delta F^l/\mathrm{R}T\right)\left\{1 - \left(\sigma_y/\sigma_a^l\right)^{3/4}\right\}^{4/3}\right] \qquad [\text{AI} - 7]$$

The temperature dependence of the shear modulus of iron is given by

$$\mu\ (\text{MPa}) = 35.36(2050 - 0.81T) \qquad [\text{AI} - 8]$$

Plasticity controlled by obstacles and lattice resistance, which are affected by the type and quantity of impurities and neutron irradiation, can be characterized in terms of the athermal stress and activation energy, determined using Eqs. [AI-6] through [AI-8].

According to Reference 15, the dislocation mobility through discrete obstacles and lattice resistance can be categorized into three groups with different activation energies: (1) for weak obstacle strength (lattice resistance and solid solution), $\Delta F < 0.2\ \mu\mathbf{b}^3$ (120 kJ/mole); (2) for a medium strength (dislocations, defect clusters, and small or weak precipitates), $0.2\ \mu\mathbf{b}^3$ (120 kJ/mole) $< \Delta F < 2\ \mu\mathbf{b}^3$ (1200 kJ/mole); (3) for a strong strength (large or strong precipitates), $\Delta F > 2\ \mu\mathbf{b}^3$ (1200 kJ/mole).

The athermal stress is inversely related to the obstacle spacing (L) by

$$\sigma_a = \kappa_o \mu \mathbf{b}/L \qquad [\text{AI} - 9]$$

where κ_o is a dimensionless dislocation-pinning factor depending on the type of obstacles, *i.e.*, solute solution (κ_s) and precipitate (κ_p).[15,17,30] The inverse obstacle spacing ($1/L$) is given by $\chi\sqrt{C_i}/\mathbf{b}$ and $\varphi\sqrt{f_v}/d$ for solid solution and precipitation, where χ and φ are constant, C_i is the solute content, and f_v and d are the volume fraction and diameter of precipitates, respectively.[21] Then σ_a is given by

$$\sigma_a = \kappa_s \chi \mu \sqrt{C_i} \text{ for solid solution} \qquad [\text{AI} - 10\text{a}]$$

$$\sigma_a = \kappa_p \varphi \mu (\mathbf{b}/\text{d}) \sqrt{f_v} \text{ for precipitation} \qquad [\text{AI} - 10\text{b}]$$

The pinning strength changes as a function of the type and size of the medium-to-strong precipitates, that is, κ_p is proportionately related to the critical angle (ω) at which a dislocation can cut an obstacle:[18,36,37]

$$\kappa_p \propto \cos\ (\omega/2) = \left\{1 - \left(\mu_p/\mu_{\text{Fe}}\right)^2\right\}^{1/2} \qquad [\text{AI} - 11\text{a}]$$

$$\kappa_p \propto \cos\ (\omega/2) = \{\ln\ (d) + 0.7\}/2\pi \text{ when } d \ll L \qquad [\text{AI} - 11\text{b}]$$

APPENDIX II

Analysis of small-angle neutron scattering

The neutron scattering intensity can be given as a function of the scattering vector ($\mathbf{q}$), which is related to the neutron wavelength (λ) and the neutron scattering angle (θ):

$$\mathbf{q} = 4\pi\ \sin\ (\theta/2)/\lambda \qquad [\text{AII} - 1]$$

To analyze precipitates induced by neutron irradiation, the difference in the neutron scattering intensity between the irradiated and unirradiated alloys ($\Delta I(\mathbf{q})$) was measured. The volume fraction of precipitates (f_v) is related to the invariant of neutron scattering intensity (Q) that is given by $\int \mathbf{q}^2 \Delta I(\mathbf{q}) d\mathbf{q}$ and the difference in the scattering length density in the matrix and precipitate ($\Delta\rho$) as given in[26,27]

$$f_v = Q/2(\pi\Delta\rho)^2 \qquad [\text{AII} - 2]$$

Assuming the atomic mass is constant, the $\Delta\rho$ can be given by superimposing the nuclear and magnetic scattering, is

$$(\Delta\rho)^2 = \left\{(\rho_n)_p - (\rho_n)_{\text{Fe}}\right\}^2 + \left\{(\rho_m)_p - (\rho_m)_{\text{Fe}}\right\}^2 \sin^2\phi \qquad [\text{AII} - 3]$$

where ϕ is the angle with respect to the direction of an applied magnetic field. Then

$$(\Delta\rho)_h^2 = \left\{(\rho_n)_p - (\rho_n)_{\text{Fe}}\right\}^2 \qquad [\text{AII} - 4\text{a}]$$

for the horizontal direction: $\phi = 0$ deg

$$(\Delta\rho)_v^2 = \left\{(\rho_n)_p - (\rho_n)_{\text{Fe}}\right\}^2 + \left\{(\rho_m)_p - (\rho_m)_{\text{Fe}}\right\}^2 \qquad [\text{AII} - 4\text{b}]$$

for the vertical direction: $\phi = 90$ deg

where the nuclear and magnetic scattering length density of the precipitate were estimated using $(\rho_n)_p = \Sigma c_i(\rho_n)_i$ and $(\rho_m)_p = \Sigma c_i(\rho_m)_i$, where c_i is the atomic fraction of each element.[28] The average volume fraction of precipitates was determined by the invariants in the horizontal and vertical direction (Q_h and Q_v), experimentally measured together with $(\Delta\rho)_h$ and $(\Delta\rho)_v$. In addition, the average diameter of precipitates (d) is derived using

$$\Delta I(\mathbf{q}) \propto \exp\ (-\mathbf{q}^2 d^2/20) \qquad [\text{AII} - 5]$$

NOMENCLATURE

P_y	yield load
t_o	thickness of small punch specimen
δ	displacement
t	time
$\sigma_{y,}$	tensile yield stress
τ_s	shear flow stress
ε and γ	tensile and shear strain, respectively
$d\varepsilon/dt$ and $d\gamma/dt$	tensile and shear strain rate, respectively
σ_a^o and σ_a^l	DO- and LR-controlled athermal stress, respectively
ΔF^o and ΔF^l	DO- and LR-controlled activation energy, respectively
$\Delta\sigma_a^o$ and $\Delta\sigma_a^l$	DO- and LR-controlled hardening, respectively

$\Delta\sigma_y^s$ and $\Delta\sigma_y^p$	hardening caused by solid solution and precipitation, respectively
μ	shear modulus
ν	Poisson's ratio
α, β, φ, and χ	dimensionless constant
ψ	gradient of yield strength with respect to absolute temperature
R	gas constant
T	absolute temperature
C_P, C_{Cu}, and C_S	atomic percent or fraction of P, Cu, and S
b	magnitude of Burgers vector
ρ_m	density of mobile dislocations
V	average velocity of dislocations
ΔG	Gibbs free energy
κ_s, κ_p	dimensionless dislocation-pinning factor related to solid and precipitation hardening
ω	critical angle at which a dislocation cut an obstacle
L	spacing of precipitates or impurities
d	diameter of precipitate
f_v	volume fraction of precipitate
q	scattering vector
$I(\mathbf{q})$	neutron scattering intensity
Q	invariant
λ	neutron wavelength
θ	neutron scattering angle
ϕ	angle with respect to the direction of applied magnetic field
$\Delta\rho$	difference in scattering length density in the matrix and precipitate

REFERENCES

1. G.E. Lucas, G.R. Oddete, P.M. Lombrozo, and J.W. Seecked: in *Effect of Radiation on Materials*, ASTM STP 870, F.A. Garner and J.S. Perrin, eds., ASTM INTERNATIONAL, West Conshohocken, PA, 1985, pp. 900–30.
2. W.J. Phythian and C.A. English: *J. Nucl. Mater.*, 1993, vol. 205, pp. 162–70.
3. K. Fukuya, K. Ohno, and H. Nakata: *Microstructural Evolution in Reactor Vessel Steels*, INSS Monograph No. 1, Institute of Nuclear Safety, Inc., Mihama, Fukui, Japan, 2001.
4. K. Onizawa and M. Suzuki: *Effects of Radiation on Materials*: *20th Int. Symp.*, ASTM STP 1405, R.S. Rosinski, M.L. Grossbeck, T.R. Allen, and A.S. Kumar, eds., ASTM INTERNATIONAL, West Conshohocken, PA, 2001, pp. 79–96.
5. J. Kameda and A.J. Bevelo: *Acta Metall.*, 1989, vol. 12, pp. 3283–96.
6. Y. Nishiyama, K. Onizawa, and M. Suzuki: *J. ASTM Inter.*, 2007, vol. 4, no. 8, JAI100690.
7. A.V. Nikolaeva, Y.A. Nikolaeva, and A.M. Kryukov: *J. Nucl. Mater.*, 1994, vol. 218, pp. 85–93.
8. G. Faulkner, S. Song, and P.E.J. Flewitt: *Metall. Mater. Trans. A*, 1996, vol. 27A, pp. 3381–90.
9. A.V. Barashev, S.I. Golubov, and D.J. Bacon: in *Microstructure Processes in Irradiated Materials*, G.E. Lucas, L.L. Snead, M.A. Kirk, Jr., and R.G. Elliman, eds., Materials Research Society, Pittsburgh, PA, 2001, p. R68.
10. J. Kameda and X. Mao: *Mater. Sci. Eng.*, 1989, vol. A112, pp. 143–49.
11. J. Kameda, Y. Nishiyama, and T.E. Bloomer: *Surf. Int. Anal.*, 2001, vol. 31, pp. 522–31.
12. Y. Nishiyama, T.E. Bloomer, and J. Kameda: in *Microstructure Processes in Irradiated Materials*, G.E. Lucas, L.L. Snead, M.A. Kirk Jr., and R.G. Elliman, eds., Materials Research Society, Pittsburgh, PA, 2001, p. R610.
13. Y. Nishiyama and J. Kameda: Japan Atomic Energy Agency, Tokai, Ibaraki, Japan, unpublished research, 2007.
14. Y. Nishiyama, K. Onizawa, M. Suzuki, J.W. Anderegge, Y. Nagai, T. Toyama, M. Hasegawa, and J. Kameda: submitted for publication.
15. H. Frost and M.F. Ashby: *Deformation-Mechanism Maps—The Plasticity and Creep of Metals and Ceramics*, Pergamon Press, Oxford, United Kingdom, 1982, pp. 6–9.
16. P. Guyot and J.E. Dorn: *Can. J. Phys.*, 1976, vol. 45, pp. 983–1016.
17. U.F. Kocks, A.S. Argon, and M.F. Ashby: *Progr. Mater. Sci.*, 1975, vol. 19.
18. K.C. Russell and L.M. Brown: *Acta Metall.*, 1972, vol. 20, pp. 969–74.
19. A. Fujii, M. Nemoto, H. Suto, and K. Monma: *Trans. Jpn. Inst. Met. Suppl.*, 1968, vol. 9, pp. 374–80.
20. R. Kasada, T. Kitao, K. Morishita, H. Matsui, and A. Kimura: *Effects of Radiation on Materials*: *21st Int. Symp.*, ASTM STP 1405, R.S. Rosinski, M.L. Grossbeck, T.R. Allen, and A.S. Kumar, eds., ASTM INTERNATIONAL, West Conshohocken, PA, 2001, pp. 237–46.
21. L.M. Brown and R.K. Ham: in *Strengthening Method in Crystals*, A. Kelly and R.B. Nicholson, eds., Elsevier, London, 1971, pp. 9–136.
22. J.M. Baik, J. Kameda, and O. Buck: *Scripta Metall.*, 1983, vol. 17, pp. 1443–47.
23. X. Mao and H. Takahashi: *J. Nucl. Mater.*, 1987, vol. 150, pp. 42–50.
24. J. Kameda and X. Mao: *J. Mater. Sci.*, 1992, vol. 27, pp. 983–89.
25. H. Matsui, S. Moriya, S. Takaki, and H. Kimura: *Trans. JIM*, 1978, vol. 19, pp. 163–70.
26. C.G. Glinka, J.C. Barker, B. Hammounda, S. Kyueger, J.S. Moyer, and W.J. Orts: *J. Appl. Cryst.*, 1998, vol. 31, p. 430.
27. *Neutron, X-Ray and Light Scattering*, P. Lindner and T.H. Zemb, eds., Elsevier Science Publishers B.V., Amsterdam, Netherland, 1991, p. 42.
28. A.J. Allen, D. Gavillet, and J.R. Weertman: *Acta Metall.*, 1993, vol. 41, pp. 1869–84.
29. K. Kitao, R. Kasada, A. Kimura, H. Nakata, K. Fukaya, K. Matsui, and M. Narui: in *Effects of Radiation on Materials*, ASTM STP 1447, M.L. Grossbeck, T.R. Allen, R.G. Lott, and A.S. Kumar, eds., ASTM INTERNATIONAL, West Conshohocken, PA, 2004, pp. 365–75.
30. J.P. Hirth and J. Lothe: in *Theory of Dislocations*, John Wiley & Sons, Inc., New York, NY, 1982, pp. 537–39.
31. V.N. Svechnikov, V.M. Pan, and A.K. Shurin: *Fiz. Metal. Metalloved.*, 1958, vol. 6, pp. 662–64.
32. W.H. Herrnstein III, F.H. Beck, and M.G. Fontana: *Trans. TMS-AIME*, 1968, vol. 242, pp. 1049–56.
33. M. Peraz, F. Ferrard, V. Massardier, X. Kleber, A. Deschamps, H. Demonestrol, P. Pareige, and G. Covarel: *Phil. Mag.*, 2005, vol. 85, pp. 2197–2210.
34. S.L. Maydet and K.C. Russell: *J. Nucl. Mater.*, 1977, vol. 64, p. 101.
35. J. Kameda and T.E. Bloomer: *Acta Mater.*, 1999, vol. 47, pp. 893–903.
36. R.O. Scattergood and D.J. Bacon: *Acta Metall.*, 1982, vol. 30, pp. 1665–77.
37. Y.N. Osetsky, D.J. Bacon, and V. Mohles: *Phil. Mag.*, 2003, vol. 83, pp. 3623–41.
38. H.P. Scott, S. Huggins, M.R. Frank, S.J. Maglio, C.D. Martin, Y. Meng, J. Santillan, and G. Williams: *Geophys. Res. Lett.*, 2007, vol. 34, p. L06302.
39. K. Onizawa: Japan Atomic Energy Agency, Tokai, Ibarakai, Japan, private communication.
40. A. Sato and M. Meshii: *Phys. Status Solidi A*, 1975, vol. 28, pp. 561–69.
41. M. Guttmann and D. McLean: in *Interfacial Segregation*, C. Johnson and J.M. Blakely, eds., ASM, Metals Park, OH, 1979, pp. 261–348.
42. M. Yamaguchi, Y. Nishiyama, and H. Kaburaki: *Phys. Rev. B*, 2007, vol. 76, pp. 035418–22.
43. D. McLean: *Grain Boundaries in Metals*, Oxford University Press, London, 1957, pp. 116–49.